

Seismic attribute selection for unsupervised seismic facies analysis using user-guided data-adaptive weights

Tao Zhao¹, Fangyu Li¹, and Kurt J. Marfurt¹

ABSTRACT

With the rapid development in seismic attribute and interpretation techniques, interpreters can be overwhelmed by the number of attributes at their disposal. Pattern recognition-driven seismic facies analysis provides a means to identify subtle variations across multiple attributes that may only be partially defined on a single attribute. Typically, interpreters intuitively choose input attributes for multiattribute facies analysis based on their experience and the geologic target of interest. However, such an approach may overlook unsuspected or subtle features hidden in the data. We therefore augment this qualitative attribute selection process with quantitative measures of candidate attributes that best differentiate features of interest. Instead of selecting a group of attributes and assuming all the selected attributes contribute equally to the facies map, we weight the interpreter-selected input

attributes based on their response from the unsupervised learning algorithm and the interpreter's knowledge. In other words, we expect the weights to represent "which attribute is 'favored' by an interpreter as input for unsupervised learning" from an interpretation perspective and "which attribute is 'favored' by the learning algorithm" from a data-driven perspective. Therefore, we claim the weights are user guided and data adaptive, as the derivation of weight for each input attribute is embedded into the learning algorithm, providing a specific measurement tailored to the selected learning algorithm, while still taking the interpreter's knowledge into account. We develop our workflow using Barnett Shale surveys and an unsupervised self-organizing map seismic facies analysis algorithm. We found that the proposed weighting-based attribute selection method better differentiates features of interest than using equally weighted input attributes. Furthermore, the weight values provide insights into dependency among input attributes.

INTRODUCTION

Seismic attributes are routinely used in the exploration, appraisal, and production stages of an oilfield life cycle with great success. However, there are many redundant attributes and many attributes with vague geologic meaning rendering them useless (Barnes, 2007). Excluding such redundant and useless attributes from the seismic interpretation workflow is important, but interpreters still face the challenge of selecting which of the remaining attributes are appropriate for a given interpretation task. Interpreters have spent a considerable amount of effort on how to select the most suitable attributes for qualitative and quantitative facies and reservoir property estimation. Chen and Sidney (1997) provide a comprehensive review on attribute selection for reservoir prediction and

monitoring, dividing attributes into wave kinematics and reservoir feature categories, and they further summarize the applicability for each attribute. Kalkomey (1997) discusses the risk of false correlation between seismic attributes and reservoir properties, and she suggests that special caution is needed when there are too few wells to correlate with too many attributes. She further suggests using only those attributes that have a physically justifiable relationship with reservoir property as predictors. Hart and Balch (2000) present a case study on predicting reservoir properties from seismic attributes with limited well control, in which they propose a suite of visual-correlation schemes to define the attributes of choice. From a more quantitative aspect, Schuelke and Quirein (1998) propose to use cross validation as a measure of prediction performance, then select attributes that lead to higher cross validation. Since then, al-

Manuscript received by the Editor 27 March 2017; revised manuscript received 12 September 2017; published ahead of production 08 December 2017; published online 01 February 2018.

¹The University of Oklahoma, ConocoPhillips School of Geology and Geophysics, Norman, Oklahoma, USA. E-mail: tao-zhao@ou.edu; fangyu.li@ou.edu; kmarfurt@ou.edu.

© 2018 Society of Exploration Geophysicists. All rights reserved.

most all the proposed alternative strategies have shared one fundamental concept, which is to select attributes that lead to the lowest validation error. Although sequential correlation (e.g., Hampson et al., 2001; Leiphart and Hart, 2001) is the most commonly used correlation method to determine the input attributes, Dorrington and Link (2004) use a genetic nonlinear inversion algorithm to automatically determine which combination of input attributes minimizes the error in neural network porosity prediction. More recently, for porosity prediction purpose, researchers explore conducting input attribute selection by incorporating model complexity into the analysis using a group method of data handling (Ahmed et al., 2010; AlBinHassan and Wang, 2011), whereas Wang et al. (2015) first use a rough set method to find the attributes that best correlate with porosity, then they use principal component analysis (PCA) to further reduce the number of input attributes to a subset of principal components.

Such prediction error-based attribute-selection methods require a relatively large number of training samples, either from well control or from interpreter-handpicked polygons defining seismic facies, providing supervision to the process. This is a supervised learning process, in which interpreters have training samples of “ground truth,” with the objective of recovering the link from input variables (e.g., seismic attributes) to a target property (e.g., lithofacies). In contrast, interpreters may also wish to discover the natural facies distribution in the data in an unsupervised manner, without introducing any bias. In this case, interpreters then use unsupervised learning, in which there is no ground truth of the target properties.

Barnes and Laughlin (2002) find that the selection of input attributes has a higher impact on the facies map than the unsupervised learning algorithm used for classification. Zhao et al. (2015) review several competing unsupervised learning algorithms and through iterative experiments find a subset of attributes to highlight different architectural elements in a turbidite system. Roden et al. (2015) use PCA to quantitatively measure the contribution of each seismic attribute to the top principal components, which in turn are used in the subsequent facies analysis. Although PCA estimates the contribution of each attribute to represent the data variability as a whole, it does not provide a means of determining which attributes best differentiate a given facies from other facies and the background behavior. Amin et al. (2017) propose a ranking framework to select the best attributes to augment supervised salt detection based on information theory. Such an information-based method is independent from the supervised learning process and therefore can be transplanted to unsupervised learning. However, it still suffers from the similar fact as PCA that it does not provide a direct measurement of attribute importance to the unsupervised learning algorithm.

One of the most commonly used seismic facies analysis algorithms is Kohonen (1982) self-organizing map (SOM). SOM is an unsupervised learning technique that projects higher dimensional multiattribute data onto a lower dimensional (usually 2D) space called a manifold, in which clusters of seismic facies are more easily defined and interpreted. In perhaps the first application of SOM to seismic data, Poupon et al. (1999) use the amplitude from a suite of 30 phantom horizons as input projected to a 1D manifold, thereby generating a facies map along a target horizon. Strecker and Uden (2002) and Coléou et al. (2003) extend these concepts to volumetric SOM analysis, in which interpreters take multiple attributes at each voxel as inputs. Since then, researchers have been investigating how to effectively recover and represent the information buried in multiple seis-

mic attributes. Matos et al. (2007) use a k -means clustering on the SOM result to reduce the number of facies. To assist in presenting SOM facies, Matos et al. (2009) display an SOM facies map using a 2D color map. Matos et al. (2011) adapt the 2D color map and use gray-level cooccurrence (GLCM) texture attributes (Gao, 2003; Di and Gao, 2017) to map Pennsylvanian channels in northern Oklahoma. Marroquín et al. (2009) introduce a visual data-mining system that displays a SOM facies map with a U-matrix (distance among SOM nodes) and parallel coordinate plot, both of which serve as quality measurements for the SOM facies map. Hu et al. (2014) and Zhao et al. (2016) introduce improvements to preserve the Euclidean distance from seismic attribute space to 2D SOM latent space. Zhao et al. (2017) constrain SOM analysis using a sedimentary cycle model to introduce spatial/temporal awareness.

At present, all multiattribute SOM analyses share one implicit assumption: Input attributes are all independent and have the same contribution/importance to the SOM facies. This assumption has greatly simplified the SOM analysis because interpreters just need to select the attributes to feed into a SOM, without specifying which of the selected attributes are more important than the others. Treating all input attributes equally is the somewhat “normal” practice in pattern recognition; unfortunately, seismic attributes are not created equally, and the importance of an attribute varies greatly with the exploration perspective. Geometric attributes (e.g., coherence) are routinely used to map discontinuities (e.g., faults) and stratigraphic edges in seismic data. In the Barnett Shale area, interpreters find coherence and curvature extremely useful when mapping the karst collapse features in the Ellenburger dolomitic formation, which pose drilling hazards to the overlying Barnett Shale formation and therefore are crucial during well path design (Sullivan et al., 2006). In contrast, Qi et al. (2014) find that spectral-decomposition attributes provide estimates of the lateral change in layer thickness and lithology, which can also map karst features in the same region. If an interpreter uses structural and spectral attributes in SOM, with the goal of mapping the facies distribution in the highly karsted Ellenburger Formation, he/she would expect these attributes to have varying degrees of impact.

In the structurally less deformed Barnett Shale reservoirs, interpreters are more interested in mapping different lithofacies, which may contain high total organic carbon or may be more susceptible to hydraulic fracturing. In this case, seismic inversion attributes (e.g., $\lambda\rho$ and $\mu\rho$) that are closely related to geomechanical behavior, are more favored by interpreters (Altamar and Marfurt, 2015). If the interpreter uses a combination of structural attributes and inversion attributes as inputs for SOM, weaker differences measured by inversion attributes may be suppressed by the stronger differences in structural attributes. One possible solution for investigating the ambiguity of the SOM facies when using suboptimal input attributes is to use a fuzzy (soft) clustering scheme, which means that instead of assigning hard class labels to each data-sample vector, one calculates the probabilities of that sample belonging to each of the classes. Generative topographic mapping is a statistical variant of SOM, which has recently been used on seismic facies analysis (Roy et al., 2014). However in this study, we stick with SOM because it is the well-established algorithm for seismic facies analysis and focus on manipulating the input attributes.

The attribute-selection system we use today is in fact simply a weighting system: If we use an attribute, its weight is one; if we reject it, its weight is zero. We therefore ask the question: Instead

of either selecting or rejecting an attribute, can we define weights that represent the significance of each input attribute in differentiating facies of interest? SOM clusters data by using either a Euclidean distance

$$r_E = \sqrt{(\mathbf{a}_1 - \mathbf{a}_2)^T \mathbf{I} (\mathbf{a}_1 - \mathbf{a}_2)}, \quad (1)$$

or a Mahalanobis (1936) distance

$$r_M = \sqrt{(\mathbf{a}_1 - \mathbf{a}_2)^T \mathbf{C}^{-1} (\mathbf{a}_1 - \mathbf{a}_2)}, \quad (2)$$

where \mathbf{a}_1 is an $N \times 1$ multiattribute data vector of N attributes, \mathbf{I} is a diagonal matrix of ones, \mathbf{a}_2 is another multiattribute data vector, \mathbf{C} is the covariance matrix of multiattribute variables, and r is the Euclidean or Mahalanobis distance between \mathbf{a}_1 and \mathbf{a}_2 . If we assume the input attributes to be independent, the Mahalanobis distance then becomes z -score, where

$$C_{ii} = \sigma_i^2 \quad (3)$$

and

$$C_{ij} = 0, \quad \forall i \neq j, \quad (4)$$

where σ_i is the standard deviation of the i th attribute. To emphasize and deemphasize the importance of a given attribute, we define a weight matrix \mathbf{W} when calculating distance in SOM:

$$r = \sqrt{(\mathbf{a}_1 - \mathbf{a}_2)^T \mathbf{W} \mathbf{C}^{-1} (\mathbf{a}_1 - \mathbf{a}_2)}. \quad (5)$$

Now, we have a diagonal matrix \mathbf{W} along with the diagonal normalization matrix \mathbf{C} used for z -score. In case \mathbf{C} is symmetric and positive definite (while not diagonal), its inverse \mathbf{C}^{-1} can be written as $\mathbf{C}^{-(1/2)} \mathbf{C}^{-(1/2)}$, and the term $\mathbf{W} \mathbf{C}^{-1}$ in equation 5 should then be replaced by $\mathbf{C}^{-(1/2)} \mathbf{W} \mathbf{C}^{-(1/2)}$. A larger value of W_{ii} means the i th attribute is more important and is weighted more in SOM, and a smaller value of W_{ii} means the i th attribute is less important, and therefore has less impact on the SOM facies map. If the diagonal contains only zeros or ones, equation 5 reduces to the traditional (binary attribute weighting) SOM, where one selects ($W_{ii} = 1$) or rejects ($W_{ii} = 0$) an attribute. In Figure 1, we show an example of randomly selected 50 sample points of two attributes from the field data used in this study to demonstrate how the weight matrix \mathbf{W} changes clusters in the data. We use k -means clustering for demonstration purpose. In this example, giving equally weighted coherence and peak-frequency attributes, k -means finds four clusters represented by the four colors in Figure 1a. These clusters are mathematically valid but somewhat less valuable geologically because clusters mainly follow coherence variations, but coherence is nothing but an on/off switch of discontinuities. Change in peak frequency may present change in lithol-

ogy and layer thickness, but the yellow cluster contains strong variation in peak frequency, which almost certainly is a mix of different geologic facies. If we weight coherence less than the peak frequency, we see a clustering that makes more geologic sense (Figure 1b), in which one cluster represents very low coherence (discontinuity), and three clusters of varying peak frequency.

We organize the rest of this paper as follows: We first present the data used in this study, which are from the Barnett Shale in north-west Texas, United States. We then introduce our definition and derivation of the weight matrix to be used for attribute selection, and we demonstrate the proposed workflow by comparing with the traditional, input attribute equally weighted SOM. We further provide a second, yet concise, field example, complementing the first experiment with another input attribute scenario. Finally, we sum up the study with conclusions.

DATA DESCRIPTION

In our field example, the Barnett Shale lies directly on top of the dolomitic Ellenburger Formation in the western region of the Fort Worth Basin (Figure 2). The Mississippian (early Carboniferous) Barnett Shale unconformably overlies the Ordovician Ellenburger Dolomite, which leaves a hiatus in the Silurian and Devonian with plenty of time for karsting of the dolomites. Going through a series of diagenetic episodes (Kupecz and Land, 1991), which include at least five karst events ranging between post Ellenburger and Early Pennsylvanian (Canter et al., 1993), the Ellenburger Formation is highly deformed, with extensive development of karst and joints that extend upward from the water-saturated Ellenburger into the Barnett Shale (Pollastro et al., 2007). Hydraulic fracturing may open these zones of weakness, so that wells intersecting karsts and diagenetically altered joints may produce a significant amount of water and therefore have to be abandoned (Qi et al., 2014).

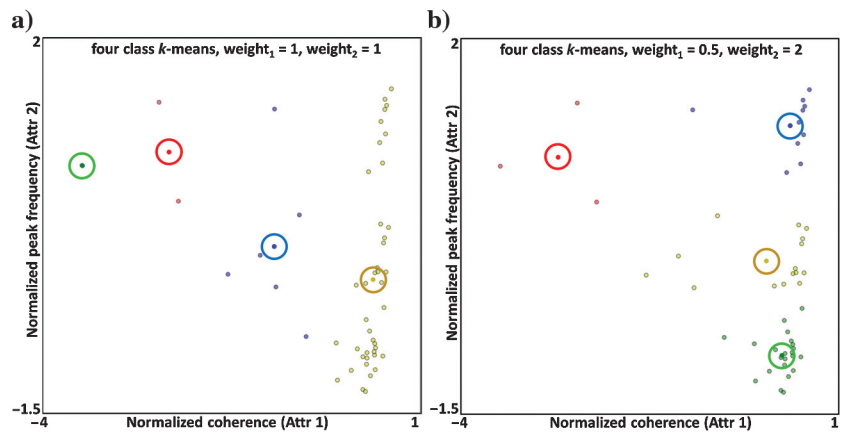


Figure 1. An example of 50 randomly selected sample points of two attributes from the field data used in this study to show the effect of attribute weights in k -means clustering. Before clustering, the attributes are normalized using a z -score algorithm. (a) Giving equally weighted coherence and peak-frequency attributes, k -means finds four clusters represented by the four colors. The yellow cluster contains a strong variation in peak frequency, which almost certainly is a mix of different geologic facies. (b) The same data samples, but now with less weight applied to coherence than the peak frequency. This clustering makes more geologic sense, with one cluster representing very low coherence (discontinuity) and three clusters of varying peak frequency. The circles denote the cluster centers.

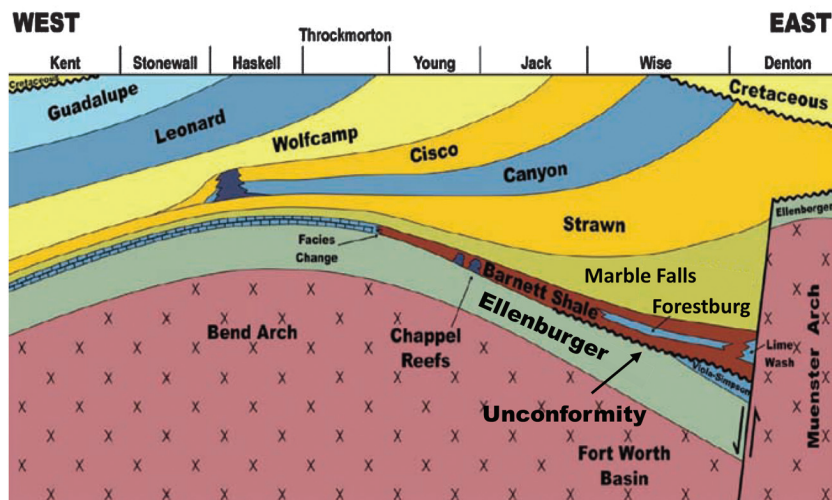


Figure 2. Stratigraphic cross section of the Fort Worth Basin. In the study area, the Barnett Shale lies unconformably on top of the dolomitic Ellenburger Formation. The seismic survey showing the Ellenburger karst is to the south of Young County in this plot (after Qi et al., 2014).

Karst-related fractures are common in the upper Ellenburger (Kerans, 1988). In this study, we focus on the upper Ellenburger. Figure 3a provides seismic amplitude section at line XX' that goes through several highly karsted regions. Proposed karst features are marked with white arrows. Figure 3b shows the seismic amplitude from a time slice at 0.75 s, which is approximately at the level of Ellenburger. Figure 3c gives the seismic amplitude from a phantom horizon (horizon A) 25 ms below the top of Ellenburger. We highlight the assumed highly karsted regions with dashed black lines in Figure 3b and 3c. Discussed in Qi et al. (2014), the seismic data are prestack time migrated with two poststack data conditioning steps applied, aiming to improving the resolution in the thin Barnett Shale and the Ellenburger Dolomite. Step one is structure-oriented filtering using a Karhunen-Loève (or principal component) filter and Kuwahara searching window (Kuwahara et al., 1976), which rejects random noises and preserves discontinuities along the structural dip. To

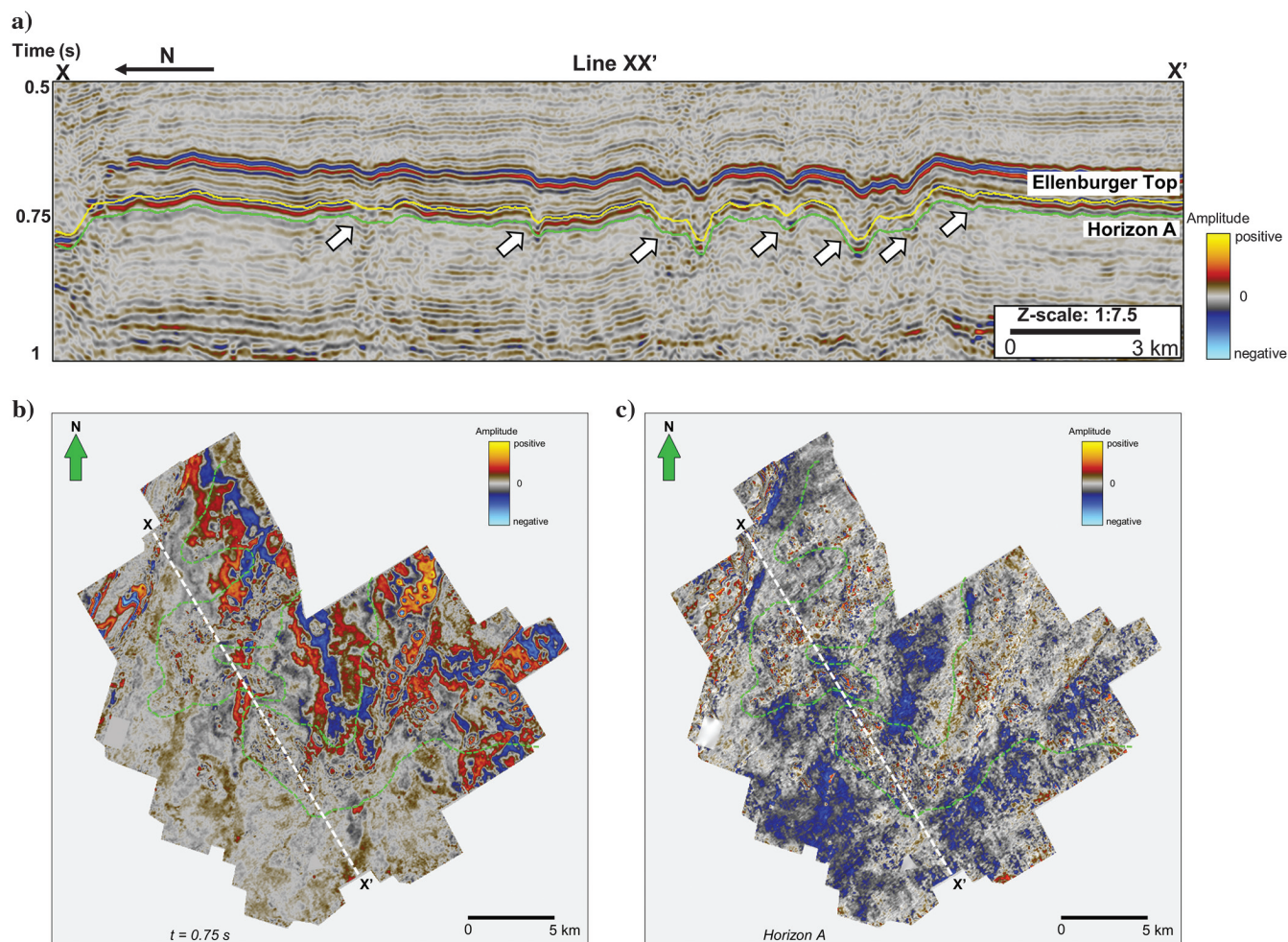


Figure 3. (a) Seismic amplitude section from line XX' (location marked in Figure 3b and 3c), (b) seismic amplitude at $t = 0.75$ s, and (c) seismic amplitude along phantom horizon A, which is 25 ms below the top of Ellenburger Formation. The white arrows mark some of the proposed karst features. The dashed green lines outline the proposed highly karsted regions.

minimize the risk of suppressing geology, a single time-variant spectral-balancing operator is then applied to the entire volume. We use spectral decomposition, geometric, and texture attributes, which are sensitive to strata thickness, lithology, and structural deformation, to illuminate the architectural elements presented in the shallow part of the Ellenburger Formation. Table 1 provides a list of attributes that are used in this study.

To study the geomorphology of the highly karsted Ellenburger Formation, we use corendered multiple attributes along horizon A, which is 25 ms below the top of Ellenburger Formation (Figures 4, 5, 6, and 7). We provide a summary of the meaning of arrow notations used in the subsequent figures in Figure 4. Karst features in the study area appear either as isolated circular to oval shape, or in a cellular network of polygonal karst. The positive (red) on the perimeter and negative (blue) in the center in structural curvature (Figure 4) define collapse features. Amplitude curvature provides a complementary image, enhancing smaller collapse features (e.g., blue arrows in Figure 5). Polygonal karst and fractures are delineated in structural and amplitude curvatures (outlined by the dashed black lines), allowing the identification of the major faults (red arrows), which compartmentalize the karst into different clusters. Modulating peak-spectral frequency by peak-spectral magnitude (Figure 6), we observe that highly karsted regions exhibit lower frequency compared with the surrounding area, possibly due to the nonspecular scattering from the chaotic reflectors. These regions are also low in peak spectral magnitude (the dimmer color in Figure 6) because a substantial amount of the reflected energy is not properly received by the receivers within the migration aperture. Besides the highly karsted regions, we also notice a shift in frequency in the less-deformed surrounding area, indicating a change in layer thickness. The yellow arrows indicate a thick layer, which should contain lower frequencies. In contrast, the orange arrows indicate a thin layer, which contains higher frequencies. Figure 7 corenders GLCM homogeneity with energy-ratio similarity. Visually, areas that are less coherent are also less homogeneous, suggesting a more rugose surface. The low GLCM homogeneity outlines the regions of karst (in red), inside which the similarity attribute provides details of the karst geometry at different scales (in black). These visual correlations of mathematically independent attributes for a given geologic feature provide an interactive, interpreter-driven means of selecting the most appropriate attributes for subsequent machine-driven classification. Naturally, we would then ask: To represent most of the attribute information in a seismic facies map, shall we just dump all these attributes into a pattern recognition algorithm, or shall we choose to honor some of them more than others? In the following sections, we demonstrate how weighting interpreter-selected input attributes differently recovers more information from the attributes.

WEIGHTING AS A MEANS FOR ATTRIBUTE SELECTION

After arriving at a reduced group of attributes, our goal is then to define the weight matrix \mathbf{W} for this group of attributes as a function of the interpreter's knowledge and attributes' contribution to

SOM. Before going into the details of deriving the weight matrix \mathbf{W} , we offer a brief review of the SOM implementation used in this study, which is built by Roy (2013). A more detailed mathematical description on this implementation is provided in Appendix A.

Table 1. Attributes used in this study and why we are using them.

Attribute	Why using this attribute
Peak spectral magnitude	Due to nonspecular reflection, substantial amount of the reflected energy is not properly received by the receivers within the migration aperture.
Peak spectral frequency	Destructive interference at karsted and faulted regions exhibits lower spectral frequency.
Most positive principal curvature Most negative principal curvature	Many karst collapse caves are in bowl shape, which produce a strong positive anomaly along the perimeter and negative anomaly at the center.
Most positive amplitude curvature Most negative amplitude curvature	Karst collapse as well as diagenetically altered joints and faults generate lateral changes in amplitude.
Energy-ratio similarity (coherence)	Karsted and faulted regions are less coherent.
GLCM homogeneity	Karsted and faulted regions are less smooth.

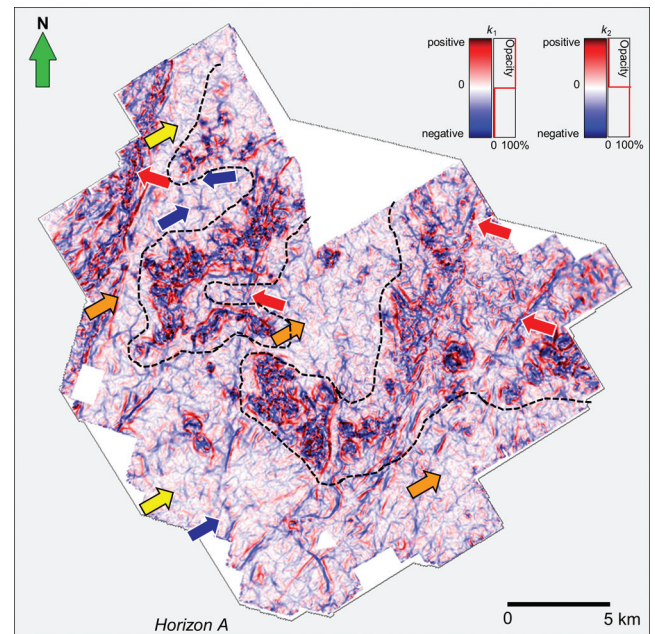


Figure 4. Corendered structural curvatures k_1 and k_2 along phantom horizon A 25 ms below the top of the Ellenburger Formation. Dashed black lines outline the extent of highly karsted regions (including polygonal karst). The red arrows can be interpreted as locations of large regional faults. The blue arrows can be interpreted as small-scale, isolated karst collapse features. The yellow arrows can be interpreted as less deformed regions of relatively thick layers, whereas orange arrows are less deformed regions of relatively thin layers.

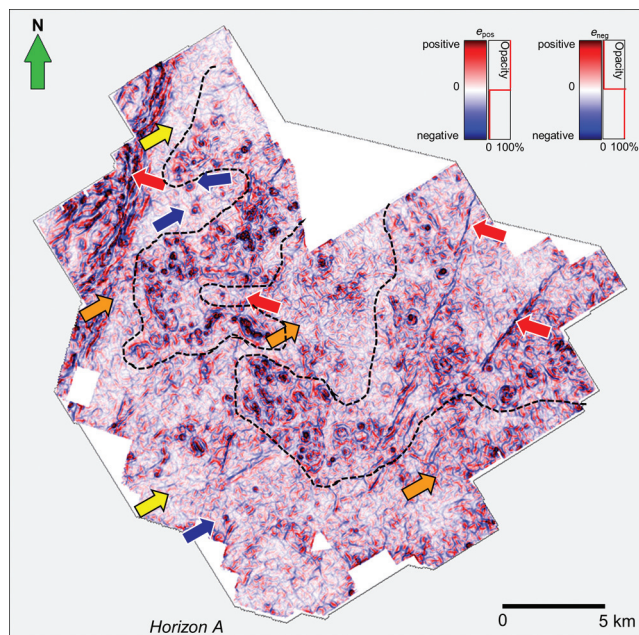


Figure 5. Corendered amplitude curvatures e_{pos} and e_{neg} along phantom horizon A 25 ms below the top of the Ellenburger Formation. The red arrows denote locations of large regional faults. Features marked by colored arrows are discussed in Figure 4. Amplitude curvature shows more details about the small-scale karst.

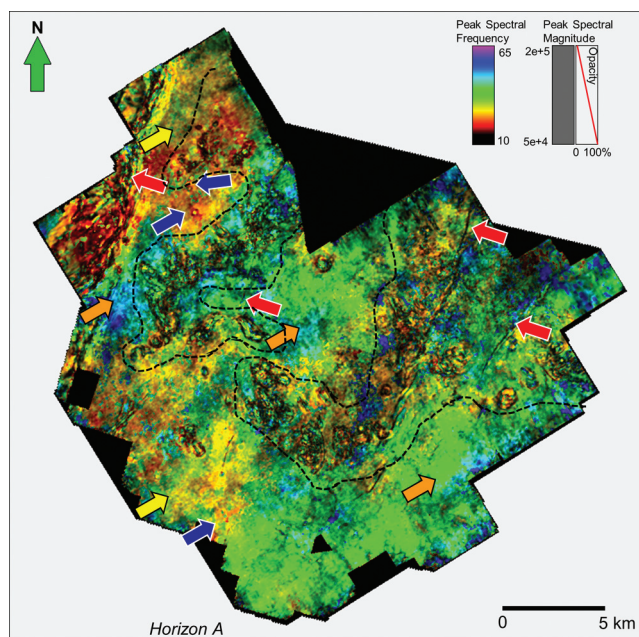


Figure 6. Peak-spectral frequency modulated by the peak-spectral magnitude along phantom horizon A 25 ms below the top of the Ellenburger Formation. The features marked by colored arrows are discussed in Figure 4. We choose a solid gray color bar with varying opacity for peak spectral magnitude to modulate the peak spectral frequency. The polygonal karst regions are of low frequency and low magnitude, possibly due to the nonspecular reflection from the highly deformed reflectors.

Starting with multiple attributes in the physical 3D space defined by x , y , and t (or z for depth), we first “transform” (or re-sort, because we are not changing any values) the data to an N -dimensional space, and each of the N -axes is defined by an attribute. The most common instance for this N -dimensional space is a 2D crossplot. For example, a $\lambda\rho$ - $\mu\rho$ crossplot that interpreters use to determine geomechanical rock properties is indeed a 2D attribute space, and each point in this space is a 2D vector of $(\lambda\rho, \mu\rho)$. Then, we use a z -score normalization to bring the attributes to the same scale. We form an $N \times N$ covariance matrix for the N attributes and calculate the eigenvalues and eigenvectors. If we project all multiattribute data vectors onto the k th eigenvector \mathbf{u}_k , we will have the k th principal component of the multiattribute data. The 2D SOM topological map is represented by SOM nodes (with two degrees of freedom), which are initialized by uniformly sampling the 2D space defined by the first two principal components. Then, we project the SOM nodes back to the N -dimensional attribute space to initialize the prototype vectors (note there is information lost during this projection if $N > 2$ because we are reconstructing N -dimensional data from the first two principal components). The objective of SOM is approximating the multiattribute data using a limited number of prototype vectors (in this case, 256 prototype vectors), and the prototype vectors are updated iteratively using the nearest data vectors. After each iteration, we update the SOM nodes by projecting the prototype vectors onto the first two eigenvectors. Finally, after a predefined number of iterations, we color code the SOM nodes using a 2D color map, based on their positions in the 2D space, find the corresponding prototype vectors in the multiattribute space, and assign the same color to the multiattribute data vectors that are closest to a prototype vector. In this way, seismic samples that have a similar attribute response have similar colors, forming a seismic facies map.

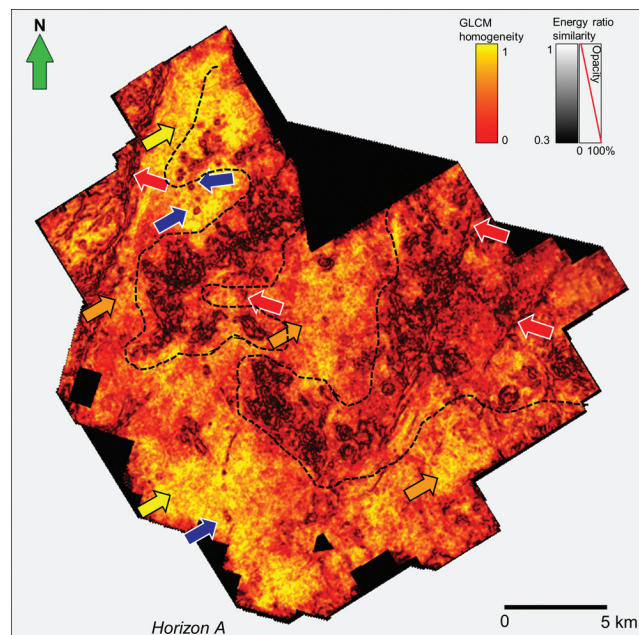


Figure 7. Corendered GLCM homogeneity and energy-ratio similarity along phantom horizon A 25 ms below the top of Ellenburger Formation. Features marked by colored arrows are discussed in Figure 4.

As previously introduced, our goal is to define a weight matrix \mathbf{W} to quantify the value of each input attribute for SOM facies analysis. We as interpreters propose that the significance of an attribute should consist of two parts, which are (1) the attributes' contribution to a SOM model and (2) what attributes are suitable as inputs for SOM. In other words, the weight of an attribute is a function of learning algorithm response and interpreter's preference. We introduce the definition of attribute weight in the rest of this section.

Inspired by Benabdeslem and Lebbah (2007), given N input attributes and J prototype vectors (which are the proxies of the 2D SOM neurons in the attribute space), we define ω_i , the i th attribute's contribution to a SOM model, as

$$\omega_i = \sum_{j=1}^J d_j \frac{|p_{ji}|}{\sum_{k=1}^N |p_{jk}|} \quad (6)$$

and

$$d_j = \frac{h_j}{M}, \quad (7)$$

where h_j is the number of multiattribute training samples that are nearest to the j th prototype vector, M is the total number of multiattribute training samples, d_j represents the density of training samples assigned to the j th prototype vector, and p_{jk} is the value of the j th prototype vector along dimension k (the dimension of the k th attribute). Physically, if a prototype vector has a very large value in the dimension of the target attribute, and a large percentage of training samples are close to this prototype vector, then the target attribute's contribution at this prototype vector is significant. Summing up over all the prototype vectors, we then arrive at the target attribute's contribution to the whole SOM model.

Unfortunately, after some tests, we conclude that this contribution ω depends on the combination of attributes, which means that the rank of contribution for a given group of attributes changes by adding a new attribute in the group. Such a phenomenon is a drawback of using PCA to initialize the SOM neurons. In our SOM implementation, the SOM neurons are initialized uniformly in the 2D space defined by the first two principal components of the input attributes. The first two principal components will change by adding

or dropping attributes from the input group; as a result, the projection from input attribute space to the 2D SOM space changes, whereas the contribution of each attribute changes as well. To ensure an overall optimal contribution measurement for a given group of attributes, we propose to use an exhaustive search over all S combinations of three or more attributes

$$S = \sum_{i=3}^N \frac{N!}{i!(N-i)!}, \quad (8)$$

and then we weight by the number of attributes in each combination and take the sum over all used combinations:

$$\hat{\omega}_i = \sum_{l=1}^S N_l \tilde{\omega}_{il}, \quad (9)$$

where ! denotes the factorial operation, S is the total number of SOM models to be searched, N_l is the number of attributes in the l th combination, $\tilde{\omega}_{il}$ is the contribution of the i th attribute to the l th SOM model, and $\hat{\omega}_i$ is the final contribution of the i th attribute to SOM. Although the proposed method involves running SOM multiple times with different input attribute combinations, it is an embarrassingly parallel problem so that the increase in computation time over traditional SOM is negligible given a sufficient amount of threads/processors. Table 2 provides the computation cost for running with equally weighted attributes (building one SOM model), adaptively weighted attributes in parallel mode (building S SOM models), and adaptively weighted attributes in sequential mode (building S SOM models).

To quantify which attributes are favored by interpreters to be used for SOM facies analysis, we first need to define an ideal facies map. Practically, an interpreter can either use different colors or delineate boundaries to define different facies. The authors favor color representation because then the boundary information becomes complementary once a color change is identified. In a facies map, one facies corresponds to one and only one label (color), so that geobodies can be extracted using these facies labels. In contrast, if we define a facies map in terms of boundaries compartmentalizing facies, we lose the information of the facies themselves. To generate

Table 2. Computation cost for SOM running with (1) equally weighted attributes in sequential mode, (2) equally weighted attributes in parallel mode, (3) adaptively weighted attributes in sequential mode, (4) adaptively weighted attributes in partial parallel mode, and (5) adaptively weighted attributes in full-parallel mode.²

Test case	Adaptive weighting?	Number of SOM models	Number of processors		Time elapsed (in s)		
			Building SOM model (s)	Final clustering	Model building	Final clustering	Total ³
1	No	1	1	1	12	572	792
2	No	1	1	24	12	220	444
3	Yes	219	1	1	2981	564	3723
4	Yes	219	1	24	2792	224	3217
5	Yes	219	24	24	137	217	550

²Within the analysis window defined by two horizons, the total amount of data vectors is approximately 35 million, from which we use 1% for building SOM models. The suboptimal computation cost reduction in the final-clustering stage is due to the fact that the parallelization conducts at the trace level. In this study, we use a very small vertical analysis window, which results in a considerable amount of communication overhead in the final clustering. The parallelization is implemented using Intel MPI.

³The total time includes the model building, final clustering, and data-preparation stages.

a map of the facies instead of facies boundaries from pattern recognition based on seismic attributes, the input attributes have to follow the trend on the facies, but not the facies boundaries, which are usually discontinuities. Sometimes, a facies is defined by the texture of the discontinuities, such as mass transport complex, syneresis, and karst. Then, we may use texture attributes to “group” such discontinuities and form a facies. In the real world, discontinuities and deformations consist of only a small portion of the seismic data; therefore, the data distribution of attributes such as coherence and curvature is highly skewed and sharp, and it can dominate in voxel-based classification methods. A window-based seismic facies classification method is proposed by Song et al. (2017); however, the authors use waveforms instead of multiple attributes. Here, we loosely define an “edge” attribute to be an attribute representing

the variation among neighboring seismic samples, and a “body” attribute to be an attribute representing a property of a seismic sample or samples within a window, which is usually along the structure dip and of cylindrical or cubical shape. Figure 8 shows an example of two attributes along a horizon slice from the Ellenburger Formation, Fort Worth Basin. The GLCM homogeneity is a texture attribute that provides a measure of the amplitude smoothness along a horizon, which is a body attribute. In contrast, the energy ratio similarity highlights edges, but it ignores changes outside the edges. Researchers in geostatistics routinely inspect histograms to determine if variables possess a distribution that satisfies the assumption for subsequent analysis and even transform a variable using quantile representation if its distribution is highly skewed (Coburn et al., 2005). Figure 8c and 8d shows histogram of these two attributes, from which we observe that the body attribute exhibits a flatter and more symmetric histogram, whereas the edge attribute’s histogram is tighter and more skewed. Based on this observation, we proposed to use the skewness and kurtosis of attributes, which measures the asymmetry and sharpness of data distribution, to quantify the interpreter’s preference of body attributes over the edge attributes.

Skewness, which is the third moment of the standard score of a variable x , is defined as

$$s(x) = \mathbb{E} \left[\left(\frac{x - \bar{x}}{\sigma_x} \right)^3 \right], \quad (10)$$

where \bar{x} is the mean of variable x , σ_x is the standard deviation, and \mathbb{E} represents the expectation. Similarly, kurtosis is the fourth moment of the standard score of a variable x and is defined as

$$k(x) = \mathbb{E} \left[\left(\frac{x - \bar{x}}{\sigma_x} \right)^4 \right]. \quad (11)$$

In practice, the skewness and kurtosis are pre-computed before determining the attribute contribution ω . After the computation of ω , we further normalize the skewness and kurtosis to range between zero and one. We weight the previously defined ω using skewness and kurtosis, and we normalize the raw weights w_i using the z-score to arrive at relative weights (the absolute value of w_i is of less interest):

$$w_i = \left(3 - \frac{|s_i| - \min_{i=1,N} |s_i|}{\max_{i=1,N} |s_i| - \min_{i=1,N} |s_i|} - \frac{k_i - \min_{i=1,N} k_i}{\max_{i=1,N} k_i - \min_{i=1,N} k_i} \right) \cdot \omega_i, \quad (12)$$

$$\hat{w}_i = \frac{w_i - \bar{w}}{\sigma_w}, \quad (13)$$

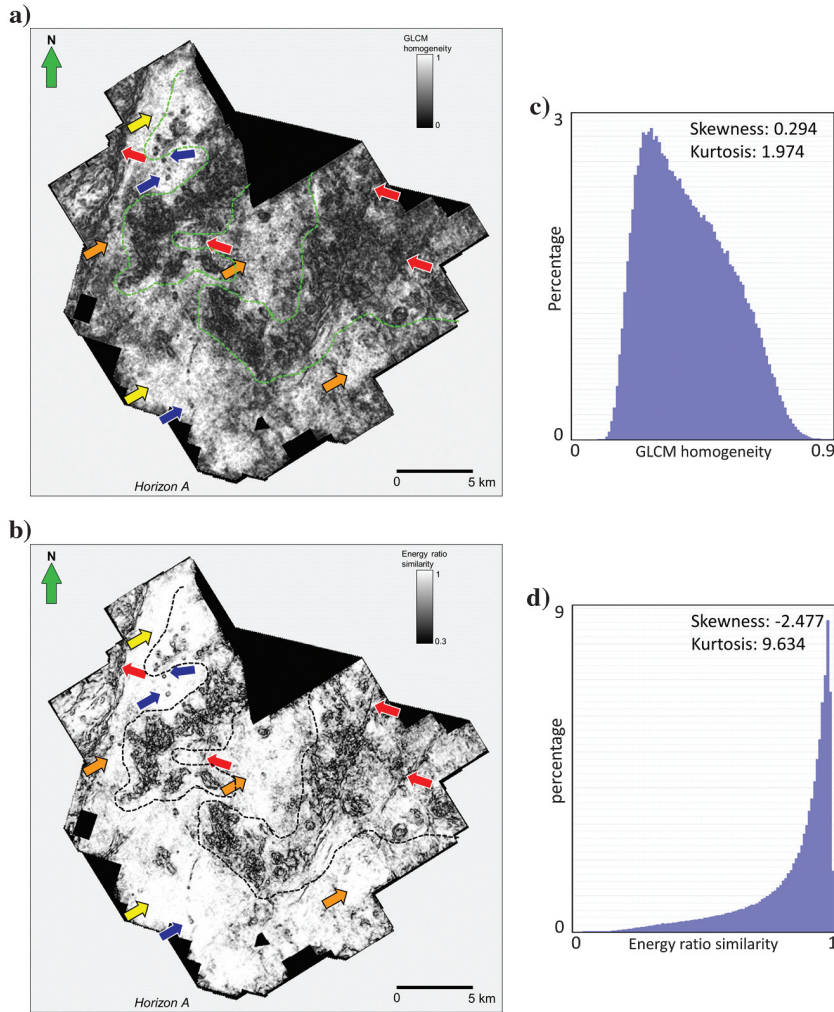


Figure 8. Phantom horizon A 25 ms below the top of Ellenburger Formation through the (a) GLCM homogeneity (with different color bars from the display in Figure 7) and (b) energy-ratio similarity volumes. Features marked by colored arrows are discussed in Figure 4. We loosely define the GLCM homogeneity as a body attribute because it represents information within a window along structural dip. It is useful for mapping the extent of the highly deformed regions. In contrast, the energy-ratio similarity is an edge attribute that highlights the boundaries. (c) The histogram of GLCM homogeneity within the analysis window. (d) The histogram of the energy-ratio similarity within the analysis window. Compared with GLCM homogeneity, the histogram of energy-ratio similarity is highly skewed and sharp.

where w_i is the weight of attribute i before z -score normalization, \bar{w} is the mean of w_i , σ_w is the standard deviation, and \hat{w}_i is the relative weight of attribute i after the z -score. In equation 12, because the skewness term and kurtosis term are normalized to range between zero and one, we assume an equal impact of skewness and kurtosis. Finally, we constrain the weight to range from zero to two using a sigmoid function, and we define the elements of the diagonal weight matrix \mathbf{W} to be

$$W_{ii} = \frac{2}{1 + e^{-\hat{w}_i}}. \quad (14)$$

Using this heuristic approach, we have defined a weighting parameter as a function of the interpreter's knowledge and the SOM response. Then, we use the distance definition in equation 5 with the updated weight matrix \mathbf{W} to run SOM a final time, and we generate the facies map. We provide a workflow summarizing the steps in Figure 9.

FIELD EXAMPLE 1: MAPPING STRUCTURAL FEATURES

We perform an SOM analysis on attributes computed within a 50 ms time window below the top Ellenburger surface to capture the structural deformation and diagenetic alteration of the shallow Ellenburger Formation, which has a direct impact on the Barnett Shale reservoir lying unconformably above. Although interaction with crossplots of two or three attributes (against x -, y -, and an additional color axis, if needed) is simple, interacting with eight attributes and an 8D crossplot is intractable. In our implementation, SOM projects this intractable 8D crossplot into a 2D space that can be visualized on a computer screen, while still preserving most of the topological and distance relationship from the original 8D space. After precomputing the attribute weight matrix as described previously, we obtain the weights of the eight input attributes and display with their corresponding histogram in Figure 10. Note that highly skewed attributes (curvature and similarity) are penalized; in contrast, body attributes are amplified. With such a penalty on curvature and similarity attributes, one may suspect that the anomalies from these attributes would have been overly mitigated. We assume that the contrast in curvature and similarity between features of interest (karst and faults, versus planar features in this example) still allows them to be classified by the SOM facies map. Most of geology is planar and continuous, such that the mean value of curvature is close to zero and the mean value of similarity close to one. In contrast, structural or curvature anomalies of interest have values several standard deviations from

the mean. Therefore, we still expect to observe the anomalies after penalizing on these attributes.

The SOM facies map with equally weighed input attributes is shown in Figure 11, and from the proposed workflow using the same group of input attribute in Figure 12. In our implementation,

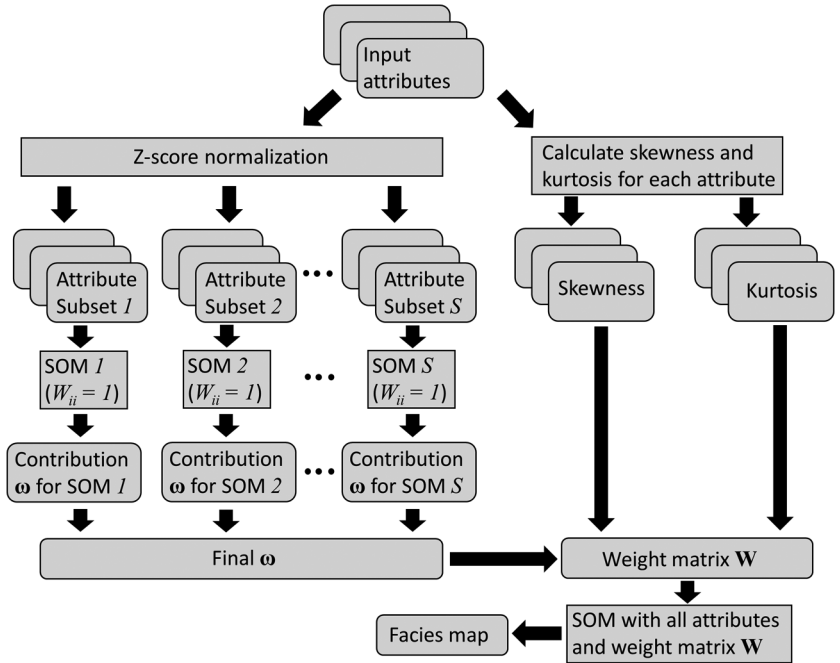


Figure 9. The proposed attribute weighting workflow. Mathematical notations are discussed in the main text.

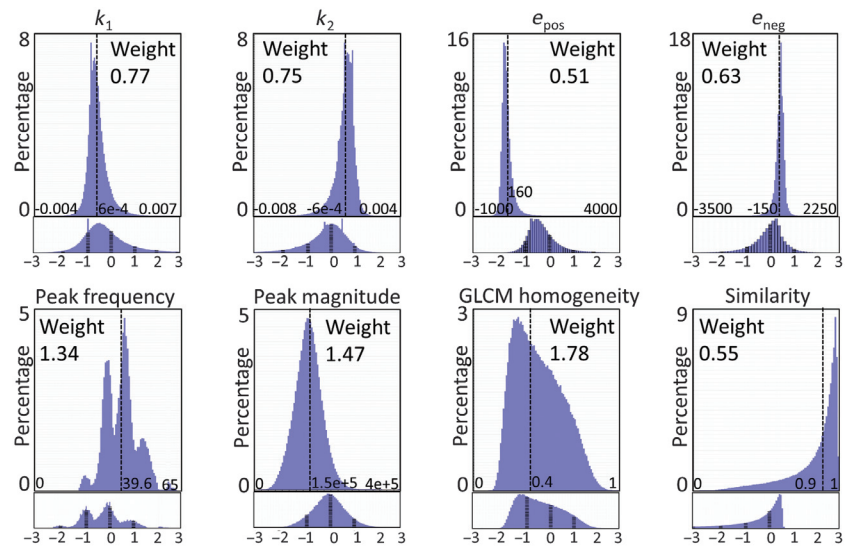


Figure 10. Histograms of the eight input attributes within the analysis window. Weights are computed using the method described in this paper. Note that histograms exhibiting high kurtosis and/or skewness are assigned lower weights, whereas those that are broader and more symmetric are assigned higher weights. Values at the bottom of each histogram mark the z -scores, and dashed lines mark values at zero, one, and two standard deviations. Note that the curvature and coherence attributes span several standard deviations.

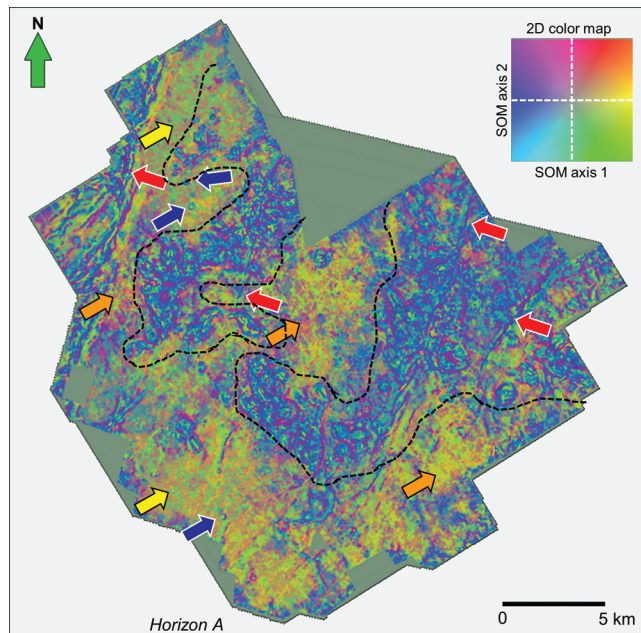


Figure 11. The SOM facies map from equally weighted attributes along phantom horizon A 25 ms below the top of the Ellenburger Formation. The features marked by the colored arrows are discussed in Figure 4. The dashed lines in the 2D color maps denote the 1D color bar used for each projection along a SOM axis to approximate the 2D color map.

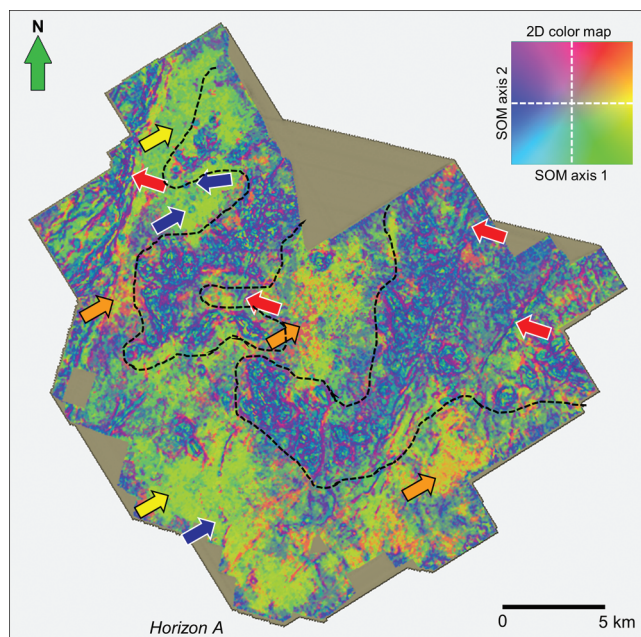


Figure 12. The SOM facies map from adaptively weighted attributes along phantom horizon A 25 ms below the top of the Ellenburger Formation. The features marked by the colored arrows are discussed in Figure 4. The dashed lines in the 2D color maps denote the 1D color bar used for each projection along an SOM axis to approximate the 2D color map.

we output the SOM facies map as two volumes, one for each axis of the projected 2D space. We then blend these two volumes together to generate a SOM facies map as shown in Figures 11 and 12. Therefore, every sample in these SOM facies map is no longer a scalar, but a 2D vector that represents the coordinates of that sample in the projected SOM 2D space. This vector representation enables us to plot the two dimensions against two 1D color bars perpendicular to each other. Using commercial crossplotting tools available in many interpretation packages provides the color bar shown in Figures 11 and 12. Such a representation has greatly enhanced the interpretation of SOM facies.

Comparing Figures 11 and 12, both SOM facies maps are able to delineate the karst, faults, and fractures equally well. This observation verifies the assumption we made earlier that adding a penalty weight does not significantly alter the curvature and similarity anomaly contributions. The polygonal karst regions are characterized by purple and cyan facies, where purple corresponds to anticlinal components and cyan to synclinal components. Compared with the corendered structural curvatures, both SOM facies maps provide details about smaller scaled karst caves that are not identifiable on structural curvatures, most of which correspond to fracture joints (blue arrows). We are also able to identify the major faults (red arrows) close to the polygonal karst regions, suggesting a tectonic control of the karst development (Khatiwada et al., 2013; Qi et al., 2014). The main difference between Figures 11 and 12 comes from regions marked with the yellow and orange arrows. In Figure 12, the yellow arrow regions are in a lime green facies, whereas the orange arrow regions are in an orange facies. In contrast, these regions look nearly identical in Figure 11, all being brownish cellular textures that somehow follow the trend on the curvature attributes. The lime green versus orange facies change

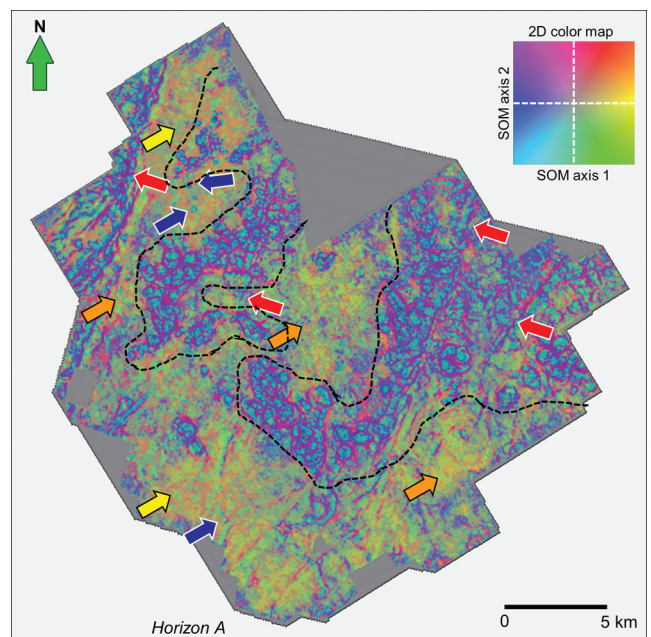


Figure 13. The SOM facies map from a subset of equally weighted attributes along phantom horizon A 25 ms below the top of the Ellenburger Formation. The features marked by the colored arrows are discussed in Figure 4. The dashed lines in the 2D color maps denote the 1D color bar used for each projection along an SOM axis to approximate the 2D color map.

in Figure 12 reflects the frequency variation found in Figure 8, where low peak-frequency regions are in lime green facies (the yellow arrows), and high-frequency regions are in orange facies (the orange arrows). The peak frequency provides information on the tuning thickness, which adds another dimension besides surface morphology. The SOM facies map from equally weighted attributes, on the other hand, does not distinguish such frequency variation clearly. After z -score normalization, the contrast in some attributes (such as curvature and similarity in this example) is much higher than the others (such as spectral decomposition attributes) and dominates the distance calculation. SOM is biased toward finding clusters in those attributes. After stretching and squeezing the distance along each attribute dimension using the precomputed weights, we are able to recover the variation in peak frequency that is otherwise buried in the strong curvature contrast. Figure 13 provides a SOM result generated from a subset of equally weighted attributes. In this example, we only use structural curvatures, peak-spectral frequency and magnitude, and GLCM homogeneity as input attributes, with the objective to better define the extent of polygonal karst while reducing the dominance of edge attributes that we previously observed when there were three more edge attributes. By eliminating the overprint from amplitude curvature and similarity, we recognize a cleaner silhouette of the polygonal karst; however, the change in frequency in the less-deformed regions is still difficult to identify. This facies map is excellent in delineating

structural deformations of karst, faults, and fractures, but it fails to properly represent frequency information.

To look for evidence of the facies discovered in Figure 12, we take four composite vertical sections (a-d) from the seismic amplitude and corender with the SOM facies (Figure 14). To allow the background seismic amplitude to come through, we modulate the opacity of the SOM facies, which leads to the faded color on the vertical sections compared with on the map along horizon A. Horizon A lies vertically at the center of the SOM analysis window, so we expect to see the same facies in Figure 12 to appear at the center (vertically) of the colored zone on vertical sections. In section (b), we use a red-white-blue color bar for seismic amplitude to better visualize the thickness change in reflectors, where the black curve marks horizon A. We see a change in the layer thickness in the two red ovals, which verifies the facies change that we previously interpreted. The karst features identified on horizon A nicely match the synclinal events on seismic amplitude profile (marked as red curves), with the perimeter in purple (which fades to magenta on the vertical sections) delineating the extent. We identify a large dome-shaped karst developed in the center of a collapse in section (d), which may be related to the compression that caused the two reverse faults on the east and west sides (blue curves). Most polygonal karst features develop along or in the vicinity of faults, and many of the smaller scale, isolated karst caves appear at joints of folds. The location of karst indicates that fractures of different scales

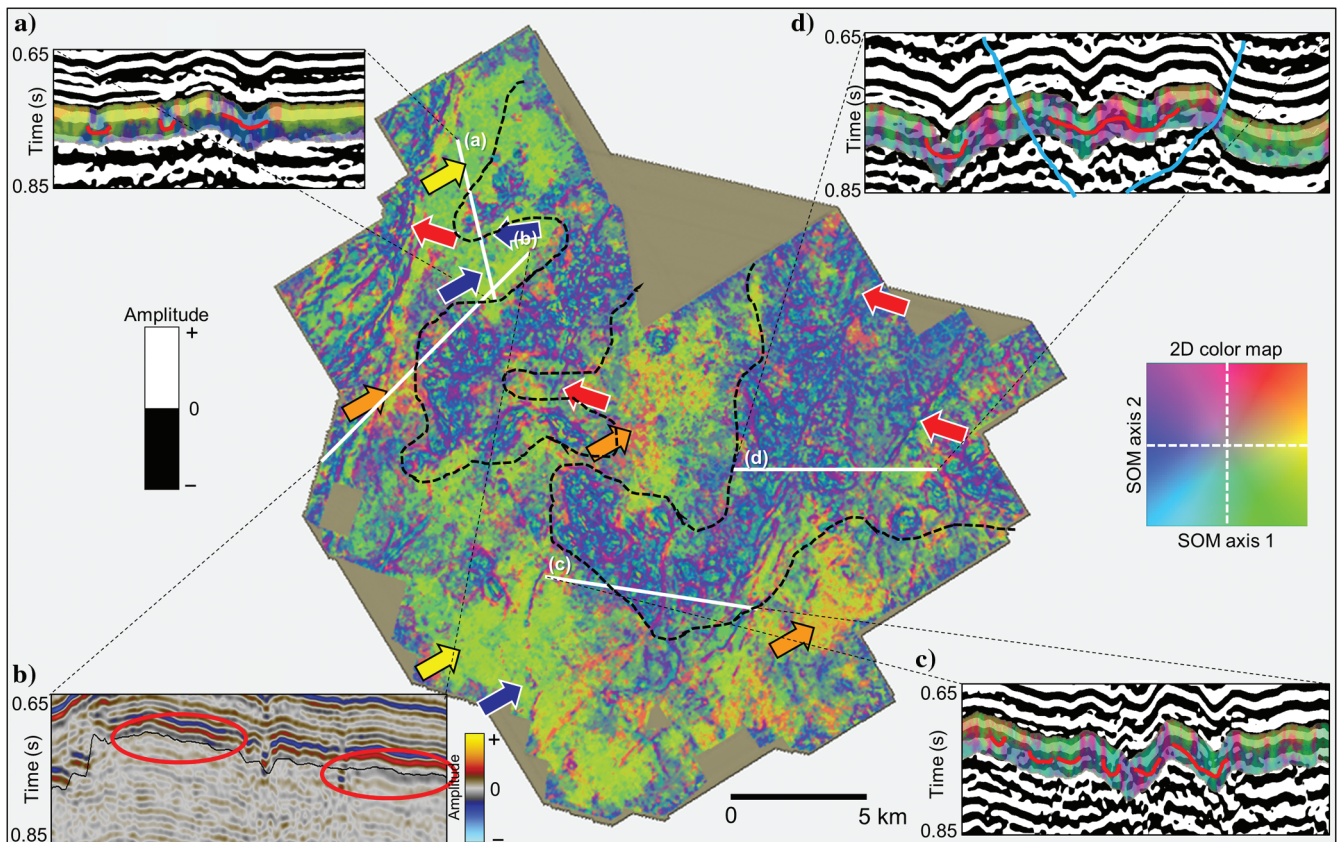


Figure 14. The SOM facies map from adaptively weighted attributes along phantom horizon A 25 ms below the top of the Ellenburger Formation. The features marked by the colored arrows are discussed in Figure 4. The dashed lines in the 2D color maps denote the 1D color bar used for each projection along a SOM axis to approximate the 2D color map. Insets (a-d) show seismic evidence of the interpreted facies.

might have accelerated the weathering and dissolution process of the Ellenburger Formation.

FIELD EXAMPLE 2: MAPPING STRATIGRAPHIC FEATURES

By now we have demonstrated that by adaptively weighting the input attribute, information from input attributes is more adequately presented in the SOM facies map. To further investigate the effectiveness of the proposed attribute weighting scheme, we provide a second example from the Barnett Shale, in which the main target is

Table 3. Input attributes and their corresponding weights used in the second Barnett Shale example. Note that the weight values of inversion attributes are consistent with attribute dependency.

Attribute	Weight
Coherent energy	0.52
Dip magnitude	0.69
Energy-ratio similarity	0.52
P-impedance	1.66
S-impedance	1.73
Lambda/mu	0.99
V_P/V_S	0.94
Poisson's ratio	0.72

to map the interbedded layers within the Barnett Shale formation overlying the Ellenburger Formation. In this example, we use structural attributes and inversion attributes as inputs to SOM, where the weights calculated using the proposed approach are provided in Table 3. Inversion attributes are closely related to the elastic properties and lithology of the rocks and are therefore effectively used to characterize shale reservoirs. On the other hand, structural attributes are useful when mapping faults and folds in the shale formation. Figure 15 shows SOM facies maps from equally weighted (Figure 15a) and data-adaptively weighted (Figure 15b) input attributes. We observe that the result from adaptively weighted attributes provides better defined layers, contain less “noise” associated with the structural attributes (black ovals), and still shows the major fault in the west of the survey. Furthermore, while increasing the weights of the inversion attributes, we also note the weights are consistent with the hierarchy of attribute dependence. The P and S impedances are two independent attributes directly obtained from seismic inversion and have the highest weights, λ/μ and V_P/V_S are calculated from P- and S-impedances and have more modest weights, and Poisson's ratio is calculated from V_P/V_S and has the lowest weight. Such weight values indirectly verify the dependency among input attributes.

CONCLUSION

In this study, we augment the attribute selection process with an attribute-weighting process for seismic facies analysis. We define the attribute weight to be a function of the SOM response and the interpreter's preference. By using such weights, information in the input attributes is more adequately represented in the SOM facies map and is less dominated by attributes with very high contrast. The weights also provide information on attribute interdependency, which may allow interpreters to understand the origin and behavior of different attributes, and in turn to select the most appropriate group of input attributes for seismic facies analysis. Being a heuristic method in nature, the proposed approach is one of the many possible ways for augmenting attribute selection; however, we believe it is the very first attempt toward using weights complementing a simple selection. We hope that the proposed approach will inspire others to add further metrics to the quantitative attribute selection problems.

ACKNOWLEDGMENTS

We thank Marathon Oil and Devon Energy for providing the seismic data used in this study. Financial support for this effort is provided by the industrial sponsors of the Attribute-Assisted Seismic Processing and Interpretation consortium at the University of Oklahoma. The prestack inversion was performed using licenses from HampsonRussell software, provided to the University of Oklahoma for research and education courtesy of CGG GeoSoftware, and all visualizations are from Petrel, courtesy of Schlumberger.

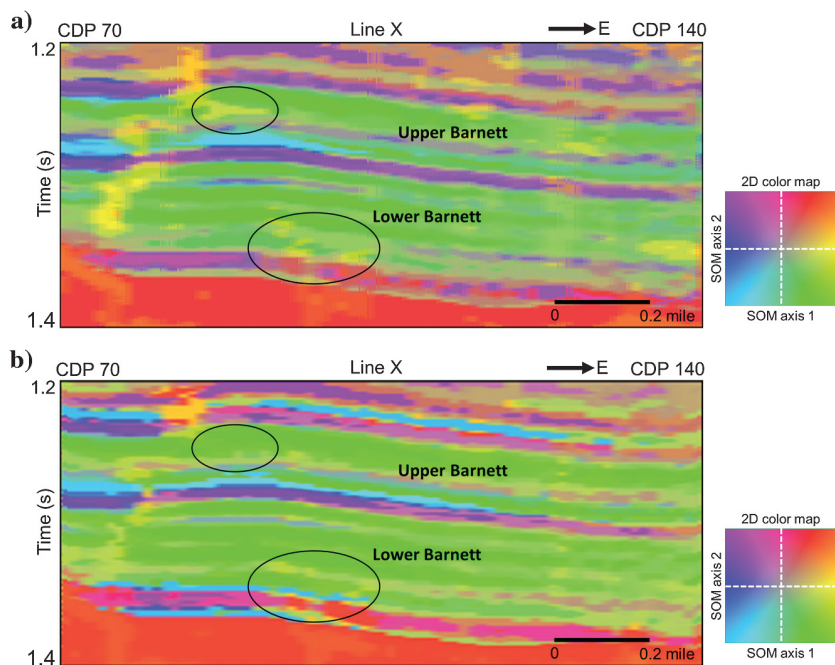


Figure 15. Vertical sections at line X from a second Barnett Shale seismic survey. (a) SOM facies map with equally weighted input attributes and (b) SOM facies map from adaptively weighed input attributes. Weights for each attribute are provided in Table 3. We notice that the layers within the shale formations are better defined in (b), and with less noise associated with structural attributes (black ovals).

APPENDIX A

MATHEMATICAL DETAILS ON THE SOM IMPLEMENTATION

For completeness, we provide the mathematical details on the SOM implementation used in this study. This implementation differs from the traditional Kohonen SOM, in that the SOM nodes in the 2D topological map are no longer restricted at the initial (regular grid) positions. Instead, they form an irregular grid to mimic the distribution of the corresponding prototype vectors in the multiattribute space. To emphasize the fact that their positions are flexible, we name the SOM nodes position vectors in this appendix. This improvement enables the color representation of facies honor the degree of similarity found in the input attributes.

Let us consider a 2D SOM represented by P prototype vectors \mathbf{p}_i , $\mathbf{p}_i = [p_{i1}, p_{i2}, \dots, p_{iN}]$, where $i = 1, 2, \dots, P$ and N is the dimension of these vectors defined by the number of input attributes (or samples for waveform classification). We first form an $N \times N$ normalized covariance matrix for the N attributes:

$$\Sigma_N = \begin{pmatrix} \sigma_1\sigma_1 & \cdots & \sigma_1\sigma_N \\ \vdots & \ddots & \vdots \\ \sigma_N\sigma_1 & \cdots & \sigma_N\sigma_N \end{pmatrix}. \quad (\text{A-1})$$

After calculating the eigenvalues λ_i and eigenvectors \mathbf{u}_i of the covariance matrix, we initialize the elliptical 2D SOM topological map as the 2D space defined by the first two eigenvectors, and we assign the position vectors (SOM nodes) \mathbf{r}_i proportionally to the first two eigenvalues. Then, we initialize a prototype vector \mathbf{p}_i as

$$\mathbf{p}_i = (\mathbf{u}_1 \quad \mathbf{u}_2)\mathbf{r}_i. \quad (\text{A-2})$$

Now, we have the initial SOM model with a set of prototype vectors \mathbf{p} and corresponding position vectors \mathbf{r} . Given a multiattribute training data vector \mathbf{a} , we compute the Euclidean distance (or alternatively, Mahalanobis distance) between vector \mathbf{a} and all prototype vectors. The prototype vector \mathbf{p}_b , which has the minimum distance to the input vector \mathbf{a} , is defined to be the “winner” or the best-matching unit (BMU), \mathbf{p}_b

$$\|\mathbf{a} - \mathbf{p}_b\| = \min\{\|\mathbf{a} - \mathbf{p}_i\|\}. \quad (\text{A-3})$$

Then, we update the BMU and its neighbors. The updating rule for the i th prototype vector inside and outside the neighborhood radius $\beta(t)$ is given by

$$\mathbf{p}_i(t+1) = \begin{cases} \mathbf{p}_i(t) + \alpha(t)h(t)[\mathbf{a} - \mathbf{p}_i(t)], & \forall \|\mathbf{r}_i - \mathbf{r}_b\| \leq \beta(t), \\ \mathbf{p}_i(t), & \forall \|\mathbf{r}_i - \mathbf{r}_b\| > \beta(t), \end{cases} \quad (\text{A-4})$$

where the neighborhood radius defined as $\beta(t)$ is predefined for a problem and decreases with each iteration (epoch) t . The functions \mathbf{r}_b and \mathbf{r}_i are the position vectors of the BMU \mathbf{p}_b and the i th prototype vector \mathbf{p}_i , respectively. We also define $h(t)$ as the neighborhood function and $\alpha(t)$ as the exponential learning rate. $h(t)$ and $\alpha(t)$ decrease with each iteration in the learning process, and they are defined as

$$h(t) = e^{-\frac{\|\mathbf{r}_i - \mathbf{r}_b\|^2}{2\beta^2(t)}} \quad (\text{A-5})$$

and

$$\alpha(t) = \alpha_0 \left(\frac{0.005}{\alpha_0} \right)^{t/T}, \quad (\text{A-6})$$

where α_0 is the initial learning rate and T is the total number of iterations. After every iteration, we update the position vectors \mathbf{r} by projecting the prototype vectors into the 2D SOM topological map space

$$\begin{cases} r_{i1}(t+1) = \mathbf{p}_i^T(t)\mathbf{u}_1, \\ r_{i2}(t+1) = \mathbf{p}_i^T(t)\mathbf{u}_2. \end{cases} \quad (\text{A-7})$$

In our implementation, in every iteration, we add a step of adjusting the position of all SOM nodes according to their distances from the current BMU in the input multiattribute space and the 2D SOM space. The adjustment rule is (Shao and Yang, 2012)

$$\mathbf{r}_i(t+1) = \mathbf{r}_i(t) + \alpha(t) \left(1 - \frac{\delta_{vi}}{d_{vi}} \right) (\mathbf{r}_v(t) - \mathbf{r}_i(t)), \quad \forall i \neq v. \quad (\text{A-8})$$

In equation A-8, $\mathbf{r}_i(t)$ is a position vector before adjustment; $\mathbf{r}_i(t+1)$ is the position vector after adjustment; $\mathbf{r}_v(t)$ is the position vector of the current BMU; and δ_{vi} and d_{vi} are the distance between a prototype vector and the current BMU in input multiattribute space and 2D SOM space, respectively. The above summarizes a full iteration in our SOM learning process. After the final iteration, we color code the position vectors using a 2D color map and assign a data vector the color of the closest prototype vector’s corresponding position vector.

REFERENCES

- Ahmed, O., R. Abdel-Aal, and H. AlMustafa, 2010, Reservoir property prediction using abductive networks: *Geophysics*, **75**, no. 1, P1–P9, doi: [10.1190/1.3298443](https://doi.org/10.1190/1.3298443).
- AlBinHassan, N., and Y. Wang, 2011, Porosity prediction using the group method of data handling: *Geophysics*, **76**, no. 5, O15–O22, doi: [10.1190/geo2010-0101.1](https://doi.org/10.1190/geo2010-0101.1).
- Altamar, R. P., and K. J. Marfurt, 2015, Identification of brittle/ductile areas in unconventional reservoirs using seismic and microseismic data: Application to the Barnett Shale: *Interpretation*, **3**, no. 4, T233–T243, doi: [10.1190/INT-2013-0021.1](https://doi.org/10.1190/INT-2013-0021.1).
- Amin, A., M. Deriche, M. A. Shafiq, Z. Wang, and G. AlRegib, 2017, Automated salt-dome detection using an attribute ranking framework with a dictionary-based classifier: *Interpretation*, **5**, no. 3, SJ61–SJ79, doi: [10.1190/INT-2016-0084.1](https://doi.org/10.1190/INT-2016-0084.1).
- Barnes, A. E., 2007, Redundant and useless seismic attributes: *Geophysics*, **72**, no. 3, P33–P38, doi: [10.1190/1.2716717](https://doi.org/10.1190/1.2716717).
- Barnes, A. E., and K. J. Laughlin, 2002, Investigation of methods for unsupervised classification of seismic data: 72nd Annual International Meeting, SEG, Expanded Abstracts, 2221–2224.
- Benabdeslem, K., and M. Lebbah, 2007, Feature selection for self-organizing map: IEEE 29th International Conference on Information Technology Interfaces, 45–50.
- Canter, K. L., D. B. Stearns, R. C. Geesaman, and J. L. Wilson, 1993, Paleogeological and related paleokarst controls on reservoir development in the Lower Ordovician Ellenburger Group, Val Verde basin, in R. D. Fritz, J. L. Wilson, and D. A. Yurewicz, eds., *Paleokarst related hydrocarbon reservoirs: SEPM Core Workshop 18*, 61–99.
- Chen, Q., and S. Sidney, 1997, Seismic attribute technology for reservoir forecasting and monitoring: *The Leading Edge*, **16**, 445–448, doi: [10.1190/1.1437657](https://doi.org/10.1190/1.1437657).

- Coburn, T. C., J. M. Yarus, and R. L. Chambers, 2005, Stochastic modeling and geostatistics: Principles, methods, and case studies: AAPG Computer Applications in Geology 5.
- Coléou, T., M. Poupon, and K. Azbel, 2003, Unsupervised seismic facies classification: A review and comparison of techniques and implementation: *The Leading Edge*, **22**, 942–953, doi: [10.1190/1.1623635](https://doi.org/10.1190/1.1623635).
- Di, H., and D. Gao, 2017, Nonlinear gray-level co-occurrence matrix texture analysis for improved seismic facies interpretation: *Interpretation*, **5**, no. 3, SJ31–SJ40, doi: [10.1190/INT-2016-0214.1](https://doi.org/10.1190/INT-2016-0214.1).
- Dorrington, K. P., and C. A. Link, 2004, Genetic-algorithm/neural-network approach to seismic attribute selection for well-log prediction: *Geophysics*, **69**, 212–221, doi: [10.1190/1.1649389](https://doi.org/10.1190/1.1649389).
- Gao, D., 2003, Volume texture extraction for 3D seismic visualization and interpretation: *Geophysics*, **68**, 1294–1302, doi: [10.1190/1.1598122](https://doi.org/10.1190/1.1598122).
- Hampson, D. P., J. S. Schuelke, and J. A. Quirein, 2001, Use of multiattribute transforms to predict log properties from seismic data: *Geophysics*, **66**, 220–236, doi: [10.1190/1.1444899](https://doi.org/10.1190/1.1444899).
- Hart, B. S., and R. S. Balch, 2000, Approaches to defining reservoir physical properties from 3-D seismic attributes with limited well control: An example from the Jurassic Smackover Formation, Alabama: *Geophysics*, **65**, 368–376, doi: [10.1190/1.1444732](https://doi.org/10.1190/1.1444732).
- Hu, C., W. Lu, and Y. Zhang, 2014, Seismic facies classification using visualization-induced self-organizing mapping: 76th Annual International Conference and Exhibition, EAGE, Extended Abstracts, doi: [10.3997/2214-4609.20140838](https://doi.org/10.3997/2214-4609.20140838).
- Kalkomey, C. T., 1997, Potential risks when using seismic attributes as predictors of reservoir properties: *The Leading Edge*, **16**, 247–251, doi: [10.1190/1.1437610](https://doi.org/10.1190/1.1437610).
- Kerans, C., 1988, Karst-controlled reservoir heterogeneity in Ellenburger Group carbonates of West Texas: *AAPG Bulletin*, **72**, 1160–1183.
- Khatiwada, M., G. R. Keller, and K. J. Marfurt, 2013, A window into the Proterozoic: Integrating 3D seismic, gravity and magnetic data to image subsurface structures in the southeast Fort Worth Basin: *Interpretation*, **1**, no. 2, T125–T141, doi: [10.1190/INT-2013-0041.1](https://doi.org/10.1190/INT-2013-0041.1).
- Kohonen, T., 1982, Self-organized formation of topologically correct feature maps: *Biological Cybernetics*, **43**, 59–69, doi: [10.1007/BF00337288](https://doi.org/10.1007/BF00337288).
- Kupecz, J. A., and L. S. Land, 1991, Late-stage dolomitization of the Lower Ordovician Ellenburger Group, West Texas: *Journal of Sedimentary Petrology*, **61**, 551–574.
- Kuwahara, M., K. Hachimura, S. Eiho, and M. Kinoshita, 1976, Processing of RI-angiocardigraphic images, in K. Preston, and M. Onoe, eds., *Digital processing of biomedical images*: Plenum Press, 187–202.
- Leiphart, D. J., and B. S. Hart, 2001, Comparison of linear regression and a probabilistic neural network to predict porosity from 3-D seismic attributes in lower Brushy Canyon channelled sandstones, southeast New Mexico: *Geophysics*, **66**, 1349–1358, doi: [10.1190/1.1487080](https://doi.org/10.1190/1.1487080).
- Mahalanobis, P. C., 1936, On the generalized distance in statistics: *Proceedings of the National Institute of Sciences of India* **2**, 49–55.
- Marroquín, I. D., J.-J. Brault, and B. S. Hart, 2009, A visual data-mining methodology for seismic facies analysis. Part I: Testing and comparison with other unsupervised clustering methods: *Geophysics*, **74**, no. 1, P1–P11, doi: [10.1190/1.3046455](https://doi.org/10.1190/1.3046455).
- Matos, M. C., K. J. Marfurt, and P. R. S. Johann, 2009, Seismic color self-organizing maps: Presented at the 11th International Congress of the Brazilian Geophysical Society.
- Matos, M. C., P. L. Osório, and P. R. Johann, 2007, Unsupervised seismic facies analysis using wavelet transform and self-organizing maps: *Geophysics*, **72**, no. 1, P9–P21, doi: [10.1190/1.2392789](https://doi.org/10.1190/1.2392789).
- Matos, M. C., M. Yenugu, S. M. Angelo, and K. J. Marfurt, 2011, Integrated seismic texture segmentation and cluster analysis applied to channel delineation and chert reservoir characterization: *Geophysics*, **76**, no. 5, P11–P21, doi: [10.1190/geo2010-0150.1](https://doi.org/10.1190/geo2010-0150.1).
- Pollastro, R. M., D. M. Jarvie, R. J. Hill, and C. W. Adams, 2007, Geologic framework of the Mississippian Barnett shale, Barnett-paleozoic total petroleum system, Bend arch-Fort Worth Basin, Texas: *AAPG Bulletin*, **91**, 405–436, doi: [10.1306/103006060008](https://doi.org/10.1306/103006060008).
- Poupon, M., K. Azbel, and G. Palmer, 1999, A new methodology based on seismic facies analysis and litho-seismic modeling: The Elkhorn Slough field pilot project, Solano County, California: 69th Annual International Meeting, SEG, Expanded Abstracts, 927–930.
- Qi, J., B. Zhang, H. Zhou, and K. Marfurt, 2014, Attribute expression of fault-controlled karst-Fort Worth Basin, Texas: A tutorial: *Interpretation*, **2**, no. 3, SF91–SF110, doi: [10.1190/INT-2013-0188.1](https://doi.org/10.1190/INT-2013-0188.1).
- Roden, R., T. Smith, and D. Sacrey, 2015, Geologic pattern recognition from seismic attributes: Principal component analysis and self-organizing maps: *Interpretation*, **3**, no. 4, SAE59–SAE83, doi: [10.1190/INT-2015-0037.1](https://doi.org/10.1190/INT-2015-0037.1).
- Roy, A., 2013, Latent space classification of seismic facies: Ph.D. dissertation, University of Oklahoma.
- Roy, A., A. S. Romero-Peláez, T. J. Kwiatkowski, and K. J. Marfurt, 2014, Generative topographic mapping for seismic facies estimation of a carbonate wash, Veracruz Basin, southern Mexico: *Interpretation*, **2**, no. 1, SA31–SA47, doi: [10.1190/INT-2013-0077.1](https://doi.org/10.1190/INT-2013-0077.1).
- Schuelke, J. S., and J. A. Quirein, 1998, Validation: A technique for selecting seismic attributes and verifying results: 68th Annual International Meeting, SEG, Expanded Abstracts, 936–939.
- Shao, C., and Y. Yang, 2012, Distance-preserving SOM: A new data visualization algorithm: *Journal of Software*, **7**, 196–203, doi: [10.4304/jsw.7.1.196-203](https://doi.org/10.4304/jsw.7.1.196-203).
- Song, C., Z. Liu, Y. Wang, X. Li, and G. Hu, 2017, Multi-waveform classification for seismic facies analysis: *Computers & Geosciences*, **101**, 1–9, doi: [10.1016/j.cageo.2016.12.014](https://doi.org/10.1016/j.cageo.2016.12.014).
- Strecker, U., and R. Uden, 2002, Data mining of 3D post-stack attribute volumes using Kohonen self-organizing maps: *The Leading Edge*, **21**, 1032–1037, doi: [10.1190/1.1518442](https://doi.org/10.1190/1.1518442).
- Sullivan, E. C., K. J. Marfurt, A. Lacazette, and M. Ammerman, 2006, Application of new seismic attributes to collapse chimneys in the Fort Worth Basin: *Geophysics*, **71**, no. 4, B111–B119, doi: [10.1190/1.2216189](https://doi.org/10.1190/1.2216189).
- Wang, Z., C. Yin, X. Lei, F. Gu, and J. Gao, 2015, Joint rough sets and Karhunen-Loève transform approach to seismic attribute selection for porosity prediction in a Chinese sandstone reservoir: *Interpretation*, **3**, no. 4, SAE19–SAE28, doi: [10.1190/INT-2014-0268.1](https://doi.org/10.1190/INT-2014-0268.1).
- Zhao, T., V. Jayaram, A. Roy, and K. J. Marfurt, 2015, A comparison of classification techniques for seismic facies recognition: *Interpretation*, **3**, no. 4, SAE29–SAE58, doi: [10.1190/INT-2015-0044.1](https://doi.org/10.1190/INT-2015-0044.1).
- Zhao, T., F. Li, and K. J. Marfurt, 2017, Constraining self-organizing map facies analysis with stratigraphy: An approach to increase the credibility in automatic seismic facies classification: *Interpretation*, **5**, no. 2, T163–T171, doi: [10.1190/INT-2016-0132.1](https://doi.org/10.1190/INT-2016-0132.1).
- Zhao, T., J. Zhang, F. Li, and K. J. Marfurt, 2016, Characterizing a turbidite system in Canterbury Basin, New Zealand, using seismic attributes and distance-preserving self-organizing maps: *Interpretation*, **4**, no. 1, SB79–SB89, doi: [10.1190/INT-2015-0094.1](https://doi.org/10.1190/INT-2015-0094.1).